# Atomic $NbO_x$ Overlayers on Palladium Nanoparticles Enhance Selective Hydrodehydroxylation

Ye Liu [a, b], Bin Zhang [b,d *], Jing Xia [c], Mark Douthwaite [d], Minghua Dong [b,h], Haiyang Yuan [e], Xiaomeng Cheng [b,h], Sen Luan [b,h], Yuxuan Wu [b,h], Zhijuan Zhao [f], Jing Tai [f], Lihua Chen [a,*], Baolian Su [a, g], Buxing Han [b,h], Huizhen Liu [b,h, *]

[a] Laboratory of Living Materials at the State Key Laboratory of Advanced Technology for Materials Synthesis and Processing, Wuhan University of Technology, Wuhan 430070, Hubei, China

[b] Beijing National Laboratory for Molecular Sciences, CAS Key Laboratory of Colloid and Interface and Thermodynamics, Center for Carbon Neutral Chemistry, Institute of Chemistry, Chinese Academy of Sciences, Beijing 100190, China

[c] Key Laboratory of Photochemical Conversion and Optoelectronic Materials, Technical Institute of Physics and Chemistry, Chinese Academy of Sciences, Beijing 100190, China

[d] Cardiff Catalysis Institute, School of Chemistry, Cardiff University, Cardiff CF103AT, UK

[e] School of Materials Science and Engineering, East China University of Science and Technology, Shanghai 200237, China

[f] Institute of Chemistry, Chinese Academy of Sciences, Beijing 100190, China

[g] Laboratory of Inorganic Materials Chemistry, University of Namur, Namur B-5000, Belgium

[h] School of Chemistry and Chemical Engineering, University of Chinese Academy of Sciences, Beijing 100049, China

* Corresponding authors: binbinz@iccas.ac.cn (B, Zhang), chenlihua@whut.edu.cn (L.Chen), liuhz@iccas.ac.cn (H. Liu).

**ABSTRACT:** The implementation of strong metal–support interactions (SMSI) is an effective design strategy that can be used to control reaction selectivity. In this study, we present evidence for the existence of SMSI between $Nb_2O_5$ and Pd, which results in the formation of an atomic thick layer of $NbO_x$ that coats the surface of Pd nanoparticles. The $NbO_x$ layer was found to profoundly affect the catalytic hydrodehydroxylation of 5-(hydroxymethyl)furfural (HMF) to 5-methylfurfural (MF). Under optimal reaction conditions, it significantly increases MF selectivity (from 6.4% to 81.0%) compared to an analogous control sample at iso-conversion. Through probing these two materials, the origin of this enhancement was attributed to the blocking of active sites responsible for the (undesirable) hydrogenation of C=O moieties. Importantly, however, the $NbO_x$ overlayer did not appear to influence the ability of the material to activate $H_2$ and preferentially dissociate C–OH on $Nb_2O_5$, which are key steps in the hydrodehydroxylation mechanism.

**KEYWORDS:** selective hydrogenolysis, strong metal–support interaction (SMSI), metal encapsulation, $Nb_2O_5$ catalysts, biomass conversion

## 1. Introduction

It has long been recognized that the structure and morphology of supported heterogeneous catalysts can have a profound effect on their physicochemical properties and thus, their performance as catalysts [1-4]. Through material design, researchers have developed several methods of fabricating strong metal-support interaction (SMSI) effects, which can drastically influence their catalytic properties. The benefit of these interactions should not be understated, as they can dramatically promote the activity [5], selectivity [6], and stability [7] of supported metal catalysts. The SMSI present in supported metal catalysts is dependent on several interactions between the metal and support. In many cases, these interactions can lead to the whole (or partial) encapsulation of the supported active metal component by the support material. This effect was initially demonstrated by Tauster *et al.* [8], who observed that structural changes could be instigated through the high-temperature reduction of $TiO_2$-supported noble metals [9,10]. Since this seminal work, further research has concluded that these effects can be observed with an extensive range of metals and supports and that the encapsulation of supported metal particles can be achieved in several ways *i.e.* thermal or chemical reduction [11-13], thermal oxidation

[14], adsorbate-mediation [15], photo exposure [16], and many others [17-19]. Qiao and his co-worker's contributions to the field have been particularly important, having developed a deep understanding of how SMSI influences the performance of various supported metal species on $CeO_2$ and $TiO_2$ supports [20,21]. Other research in this field has confirmed that these overlayers can influence the electronic properties of the supported metal component, thus, influencing how they interact with chemical substrates [22-24]. Xu *et al.* demonstrated this neatly with Ni-$TiO_2$ materials, that were prepared from a NiTi-layered double hydroxide precursor. The authors demonstrated that an increased electron density at interfacial Ni sites correlated with increased $TiO_x$ coverage, which promoted their performance in the water gas shift reaction [25].

The utilization of biomass presents an extremely challenging area of research, which is typically attributed to the intricate and diverse nature of the various feedstocks involved. Most of them possess a large proportion of oxygen which, from a valorization perspective, can be advantageous [26]. 5-(hydroxymethyl)furfural (HMF), a central platform chemical, has received immense attention due to its versatility in yielding a diverse array of value-added chemicals and liquid fuels [27-42]. HMF possesses three distinct functional moieties (hydroxyl, carbonyl/aldehyde, and furan ring), enabling diverse catalytic conversion reactions into various bio-derived products. State-of-the-art works are exemplified by selective deoxygenation to 2,5-dimethylfuran (DMF) [39] and 5-methylfurfural (5-MF) [34], hydrogenation to 2,5-bis(hydroxymethyl)furan (BHMF) [28] and 2,5-bis(hydroxymethyl)tetrahydrofuran (BHTMF) [28,40], and oxidation into 5-di(formyl)furan [41], 2,5-furandicarboxylic acid [42]. 5-methylfurfural (MF) is a high-value chemical intermediate [35,,42], which can be served as a food additive that provides flavor and aroma to various food products [27]. Additionally, MF serves as an intermediate in the production of agrochemicals and a precursor in the synthesis of specific natural anti-cancer products [43-46]. The broad range of applications underscores the selective conversion of HMF to MF is of critical importance. However, from a catalyst design perspective, it can complicate things, making reaction selectivity more difficult to control. This is particularly problematic with transformations that require selective hydrogenation because multiple reducible functional groups are typically present.

To date, our research group has successfully developed isolated $Pt_1/Nb_2O_5$ single-atom catalysts for highly efficient selective hydrogenolysis of HMF, with a >99% yield of MF [47]. However, precise and controllable synthesis for single-atom catalysts poses a significant challenge. Additionally, the presence of nanoparticles, resulting from the aggregation of single metal atoms during the reaction or catalyst preparation process, can adversely affect the catalytic performance. Recently, Ahmad et al. have developed an N-functionalized graphene-supported Mn nanoparticulate catalyst, through a high-temperature quenching process at 900°C, which demonstrated an outstanding 5-MF selectivity with complete conversion of HMF [48]. Chen et al. have developed an Au/$TiO_2$ catalyst with a diameter of 20 nm for selective hydrogenolysis of HMF, but the catalyst faces challenges in higher temperature reaction conditions of 230 °C for MF production [49]. Therefore, developing heterogeneous catalysts with metal nanoparticles for efficient selective hydrogenolysis of HMF to MF is an appealing area of research. In this regard, supported metal catalysts featuring strong metal-support interactions (SMSI) could be beneficial. Previous studies have shown that $Nb_2O_5$ materials are effective at activating and breaking C-O bonds in biomass derivatives [50]. While SMSI effects have been observed in $Nb_2O_5$-based heterogeneous catalysts with improved performance [51-57], the direct visual evidence of these effects originating from SMSI remains unclear. Given that the desired transformation involves selective hydrogenolysis of the C-O bond while preserving the C=O bond and furan ring, this reaction serves as an excellent model to investigate the SMSI effects of $Nb_2O_5$-supported catalysts [34]. The occurrence of the classical SMSI effect is highly dependent on the treatment temperature in a reducing atmosphere, and high-temperature oxidation treatment can restore the catalyst to its initial state.

Herein, we demonstrate the successful encapsulation of Pd nanoparticles with atomic-layer $NbO_x$ by treating $Nb_2O_5$-supported Pd material with hydrogen. The extent of $NbO_x$ coverage was found to be significantly influenced by the thermal reduction conditions experienced by the material, leading to a notable impact on the selectivity of HMF hydrodehydroxylation. The optimized catalyst showed good performance for the chemoselective hydrodehydroxylation of HMF with 81.0% selectivity for MF (molar percentages). This straightforward SMSI approach offers a promising platform for further investigations aimed at fine-tuning selectivity in biomass conversion.

## 2. Experimental section

### *2.1. Chemicals*

Cetyl-trimethyl-ammonium bromide (CTAB, 99%, Sigma-Aldrich), Niobium(V) oxalate hydrate (99%, Acros), $PdCl_2$ (59% Pd, Acros), $PtCl_4$ (>99.0%, Acros), $RuCl_3 \cdot 3H_2O$ (35-40%Ru, Acros), and $RhCl_3 \cdot 3H_2O$ (38.5-45.5%Rh, Alfa Aesar). Tetrahydrofuran (AR), 5-hydroxymethylfurfural (AR), 2,5-dimethylfuran (AR), 5-methylfurfural (AR), 5-methylfurfuryl alcohol (AR), 2,5-bis(hydroxymethyl)furan (AR), 2,5-bis(hydroxymethyl)tetrahydrofuran (AR), $NaBH_4$ (AR), and dodecane (AR) were purchased from Acros, J&K, and Sinopharm Chemical Reagent Co. Ltd. $H_2$ (>99.99%), Ar (>99.99%), $H_2$/Ar (10%), and CO (>99.99%) were supplied by Beijing Analytical Instrument Company. Ultrapure water was used in the experiments. All chemicals were used without further purification.

### *2.2. Catalyst preparation*

Niobium oxide was prepared according to the previous hydrothermal sol-gel method [47]. In a typical synthetic process of $Pd/Nb_2O_5$, 200 mg of $Nb_2O_5$ powder was dispersed in 50 mL of deionized water with vigorous stirring. The corresponding amount of $H_2PdCl_4$ in dilute HCl aqueous solution (6.6 $mg_{Pd}$/ml) was added drop-wise into the suspension liquid under stirring. After stirring for 2 h, the appropriate amount of $NaBH_4$ (1:20 $g_{Pd}/g_{NaBH4}$) was added and stirred for 6 h. The solution was filtered and washed with deionized water three times (3 × 30 mL) and ethanol twice (3 ×30 mL). Then the recovered solid was dried at 80 °C overnight. The obtained catalysts were denoted as $Pd/Nb_2O_5$. $Pd/Nb_2O_5$-TH (T=300,400,500,550,600°C) was obtained by reducing $Pd/Nb_2O_5$ at various temperatures for 4 hours in a 10% $H_2$/Ar atmosphere. $Pd/Nb_2O_5$-500H catalyst was re-oxidized by calcination at 300 °C for 1 h in air, denoted as $Pd/Nb_2O_5$-500H-300O. $Nb_2O_5$-supported Ru, Rh, and Pt catalysts were synthesized using the above method, except the metal precursor is different.

### *2.3. Hydrodehydroxylation reaction.*

In a typical run, the 5-hydroxymethylfurfural (12.6 mg), catalyst (10.0 mg), dodecane (15.1 mg), and tetrahydrofuran (2ml ) were loaded into a hydrogenation kettle with a magnetic rotor. The hydrogenation kettle employed in this system is a high-temperature and high-pressure tolerant vessel with a capacity of approximately 16 ml. The reactor was filled with 1.0 MPa high purity $H_2$ (> 99.99 %, Beijing Analytical Instrument Company) to replace the residual air in the reactor, evacuated three times, and then rushed into a given hydrogen pressure value (1.0/2.0/3.0/4.0 MPa) and sealed. After that, the reactor was heated to the specified temperature (160 °C) while maintaining a stirring speed of 600 rpm. After reaching the set reaction time, the reactor was taken out, put in an ice bath, and cooled to room temperature. Then the reaction gas was released, and the reaction liquid and the catalyst solid-liquid two-phase were separated. The quantitative analysis of the liquid products was conducted using a GC (Agilent 7890B) equipped with a flame ionization

detector (FID) and an Innowax capillary column (0.25 mm in diameter, 30 m in length). Identification of the products and reactant was done using a GC–MS (Agilent 7890B 5977 B, Innowax capillary column (0.25 mm in diameter, 30 m in length) as well as by comparing the retention time with dodecane as the internal standard in GC tests. To calculate the conversion of HMF and the selectivity of MF, an internal standard method based on GC data was employed. The initial molar amount of HMF is denoted as $n_0$, the molar amount after the reaction is represented as $n_1$, and the resulting product MF's molar amount is indicated as $n_2$. Other products are calculated in the same way as MF. The conversion and selectivity formulas are as follows:

$$\text{Conversion (\%)} := \frac{(n_0 - n_1)}{(n_0)} \times 100\% \quad (1)$$

$$\text{MF Selectivity (\%)} := \frac{(n_2)}{(n_0 - n_1)} \times 100\% \quad (2)$$

*2.4. Characterizations*.

Aberration-corrected high-angle annular dark-field scanning transmission electron microscopy (AC-HAADF-STEM), and electron energy loss spectroscopy (EELS) were obtained on JEM-ARM300F operated at 300 kV equipped with a Gatan OneView fast imaging camera and Quantum Dual EELS imaging system. The chemical compositions of the covering layer of Pd NPs were characterized by directly putting an electron beam on the boundary of Pd NPs in a STEM mode. Before measurements, the samples were ultrasonically dispersed in ethanol, and then a drop of the solution was put onto the carbon film supported by a copper grid. High-resolution transmission electron microscopy (HRTEM) images and scanning transmission electron microscopy (STEM) mappings were obtained using a JEOL-2100F electron microscope operated at 120 kV. Field emission transmission electron microscope JEM-F200 was operated at 200 kV. The CO-probe Fourier transforms infrared spectroscopy (CO-FTIRS) was performed in FOLI10-R-T infrared spectrometer equipped with a DLaTGS detector, made by INSA Co. Ltd. The CO-FTIRS experiments were operated with a transmission mode at a resolution of 4 $cm^{-1}$ and scanned at speed of one spectrum per minute. Before CO adsorption, all catalysts were treated in 10% $H_2$/Ar at 200 °C for 30 min. After cooling to room temperature, the background spectrum was recorded. And then pure CO was introduced into the in-situ reaction cell, and the spectra were collected continuously until unchanged. Subsequently, pure Ar was introduced to remove the gas phase CO until gaseous CO completely disappeared, and the spectra were recorded during the process. In situ, FT-IR spectra were conducted in an FOLI10-R-T infrared spectrometer equipped with a DLaTGS detector. Ultralow-temperature CO-Fourier transforms infrared spectroscopy (LT-CO-FTIR) was conducted at -150 °C in a CO pulse supply from $10^{-5}$ bar on the in-situ transient platform CRCP-7070 in Tianjin Xianquan company. X-ray photoelectron spectroscopy (XPS) was conducted on an X-ray photoelectron spectrometer (USA, Thermo Fischer, ESCALAB 250Xi) equipped with Al Kα excitation source (1486.8 eV), using C1s (284.8 eV) as the standard. The actual Pd loadings of all catalysts were determined by an inductively coupled plasma optical emission spectrometer (ICP-OES). X-ray diffraction (XRD): Powder XRD was performed at a Smart Lab X-ray diffractometer using Cu-Kα radiation (λ = 0.15432 nm), operating at 40 kV and 40 mA. Hydrogen temperature programmed reduction ($H_2$-TPR), hydrogen temperature programmed desorption ($H_2$-TPD), and metal dispersion were characterized on Auto Chem HP 2950 (USA, Micromeritics Instrument Corporation). Electron paramagnetic resonance (EPR) was characterized by Bruker A300-10/12. $N_2$ adsorption/desorption isotherms were tested on Micro 2020HD88(ASAP 2460).

*2.5. Calculations.*

All density functional theory (DFT) calculations were performed with the VASP code [58], using the Perdew-Burke-Ernzerhof (PBE) functional within the generalized gradient approximation (GGA) [59]. The core-valence electron interaction was represented by the project-augmented wave (PAW) method [60]. The valence electrons were expanded in a plane-wave basis set with a cutoff energy of 450eV. The Broyden method was employed for geometry optimization until the maximal force on each relaxed atom was less than 0.05 eV/Å. Both Pd(111) and $Nb_2O_5$(001) surfaces were modeled by a four-layer slab model with a vacuum of 15 Å, which corresponds to a k-points mesh of 2×2×1, respectively. The constrained minimization method was used to search the transition states (TSs) [61].

## 3. Results and discussion

### *3.1. Structural characterizations*

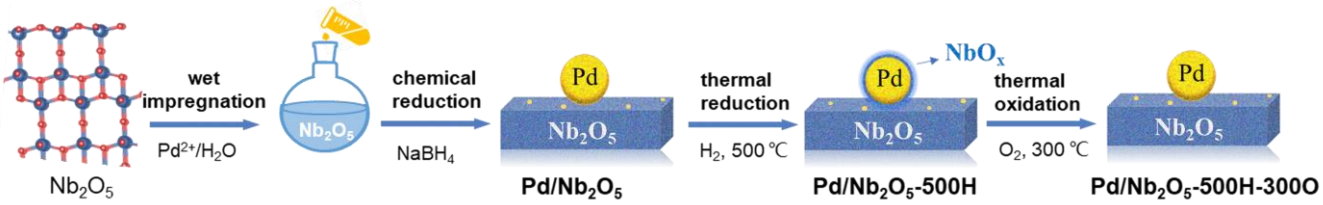


**Fig. 1.** Illustrative representation of the preparation process to produce the series of $Nb_2O_5$-supported Pd catalysts used in this study.

To begin our investigation, $Nb_2O_5$ was prepared using a hydrothermal sol-gel method [47], using cetyl-trimethyl-ammonium bromide as the surfactant (Methods and Fig. S1). Aliquots of the resultant $Nb_2O_5$ were subsequently used as a support for the synthesis of $Pd/Nb_2O_5$ material. It was prepared through the impregnation of $H_2PdCl_4$ precursor, followed by a chemical reduction with $NaBH_4$ (Table S1). The $Pd/Nb_2O_5$ material was subsequently annealed at 500°C in flowing 10%$H_2$/Ar, denoted as $Pd/Nb_2O_5$-500H, as presented in Fig. 1. $Pd/Nb_2O_5$ and $Pd/Nb_2O_5$-500H were examined by high-angle annular dark-field scanning transmission electron microscopy (HAADF-STEM) and energy dispersive spectroscopy (EDS). As shown in Fig. 2a-e, there was no evidence of Nb observed in the overlapping region of Pd in $Pd/Nb_2O_5$ catalyst. A trace amount of O however was observed in this region, which we attribute to surface Pd oxidation. On the contrary, both Nb and O were observed in a similar region to Pd after exposing this material to a reductive thermal treatment ($Pd/Nb_2O_5$-500H). This suggests that this treatment results in the growth of an $NbO_x$ layer over the Pd NPs (Fig. 2f-j). To confirm that the overlayer was induced from SMSI, an aliquot of this material was subjected to an additional thermal oxidation treatment. Following its reduction at 500 ºC, it was subsequently heated to 300 ºC under air, denoted as $Pd/Nb_2O_5$-500H-300O. As shown in Fig. 2k-o, there was no evidence to suggest that Nb was still present on the surface of the Pd. This reversible behavior of overlayers via reduction-oxidation treatment is characteristic of classic SMSI [62]. We attribute the large remaining proportion of O present in this material to the formation of PdO during the subsequent calcination procedure, which was confirmed by X-ray diffraction (XRD) (Fig. S2).

To obtain a deeper understanding of the $NbO_x$ overlayer, the $Pd/Nb_2O_5$, and $Pd/Nb_2O_5$-500H materials were subsequently probed by atomic-resolution microscopy and electron energy loss spectroscopy (EELS), and CO-probe Fourier transform infrared spectroscopy (CO-FTIRS). Three regions in the vicinity of the Pd NPs were selected and examined by atomic-scale Nb EELS and are representative

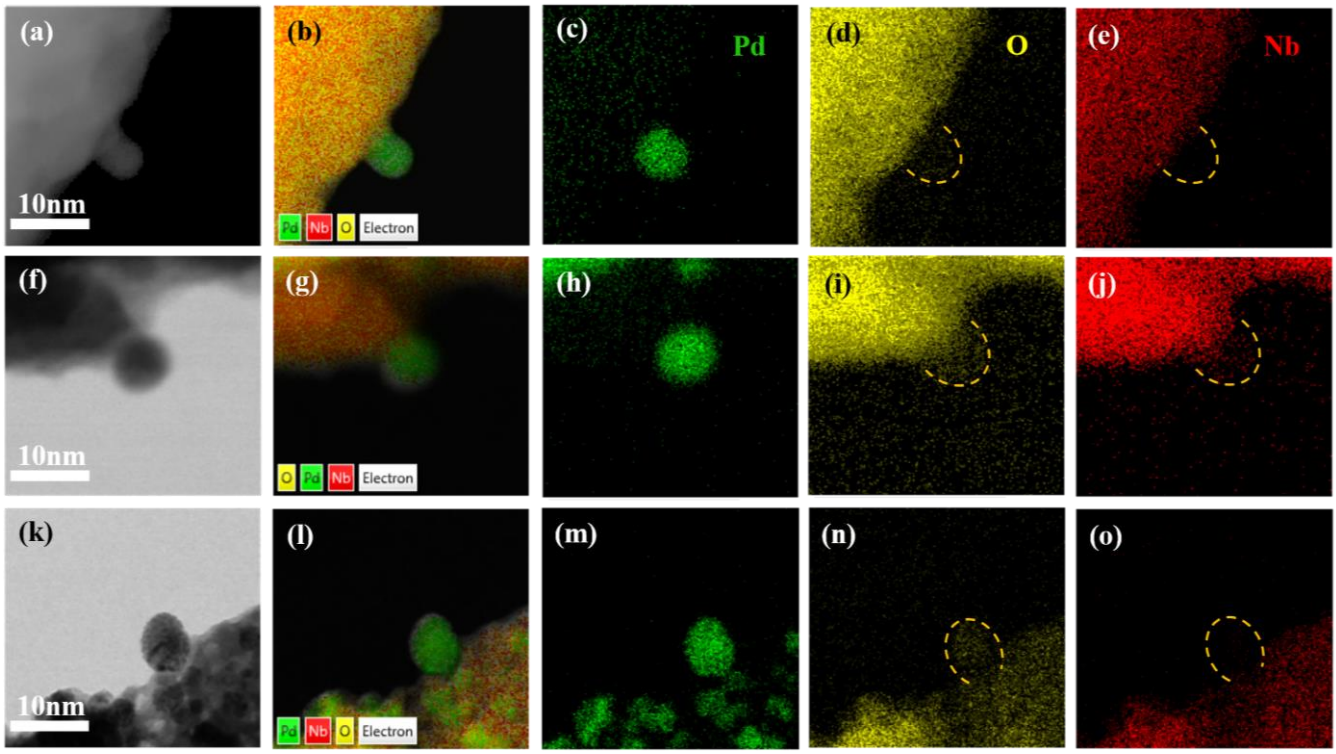


**Fig. 2.** HAADF-STEM images and EDS mappings of Pd, O, and Nb elements on $Pd/Nb_2O_5$ (a-e), $Pd/Nb_2O_5$-500H (f-j), and $Pd/Nb_2O_5$-500H-300O (k-o).

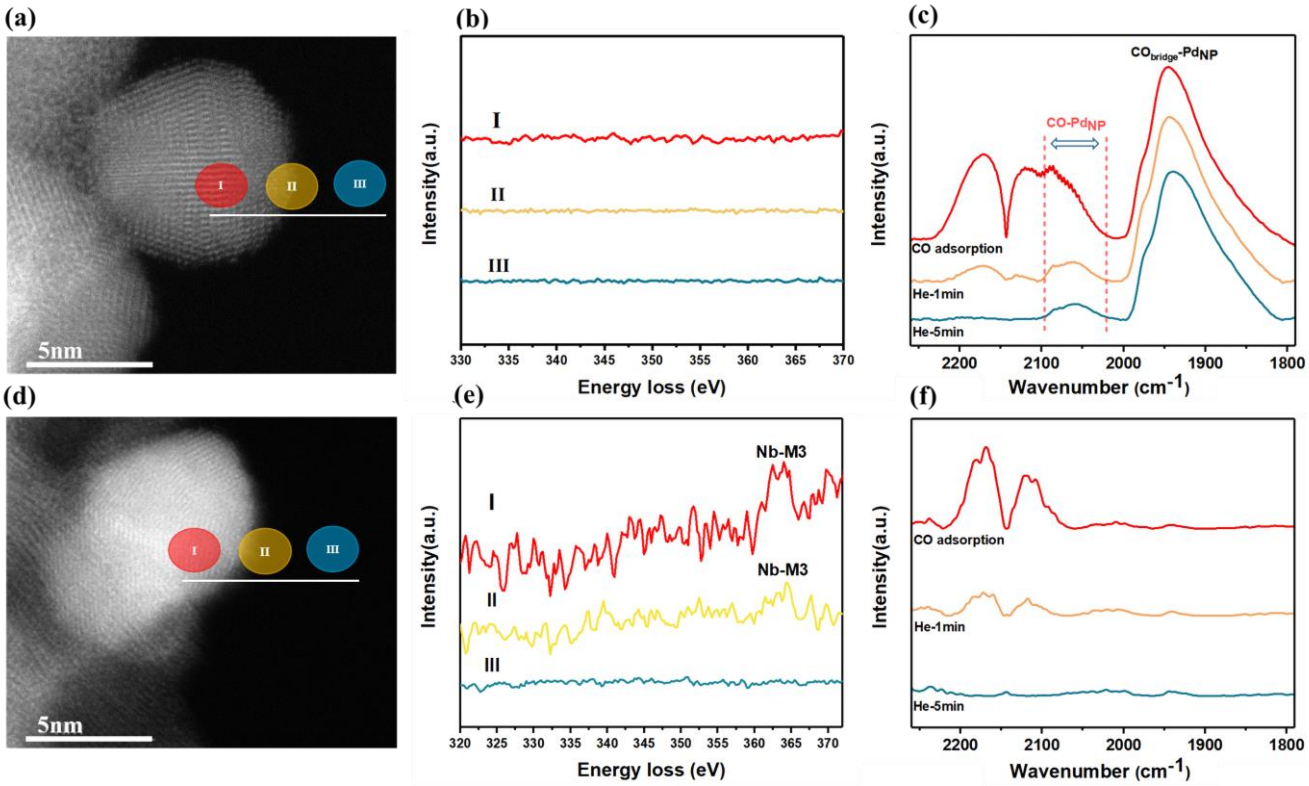


**Fig. 3.** AC-HAADF-STEM images, EELS spectra, and CO-FTIRS spectra of $Pd/Nb_2O_5$ (a-c), and $Pd/Nb_2O_5$-500H (d-f) at room temperature.

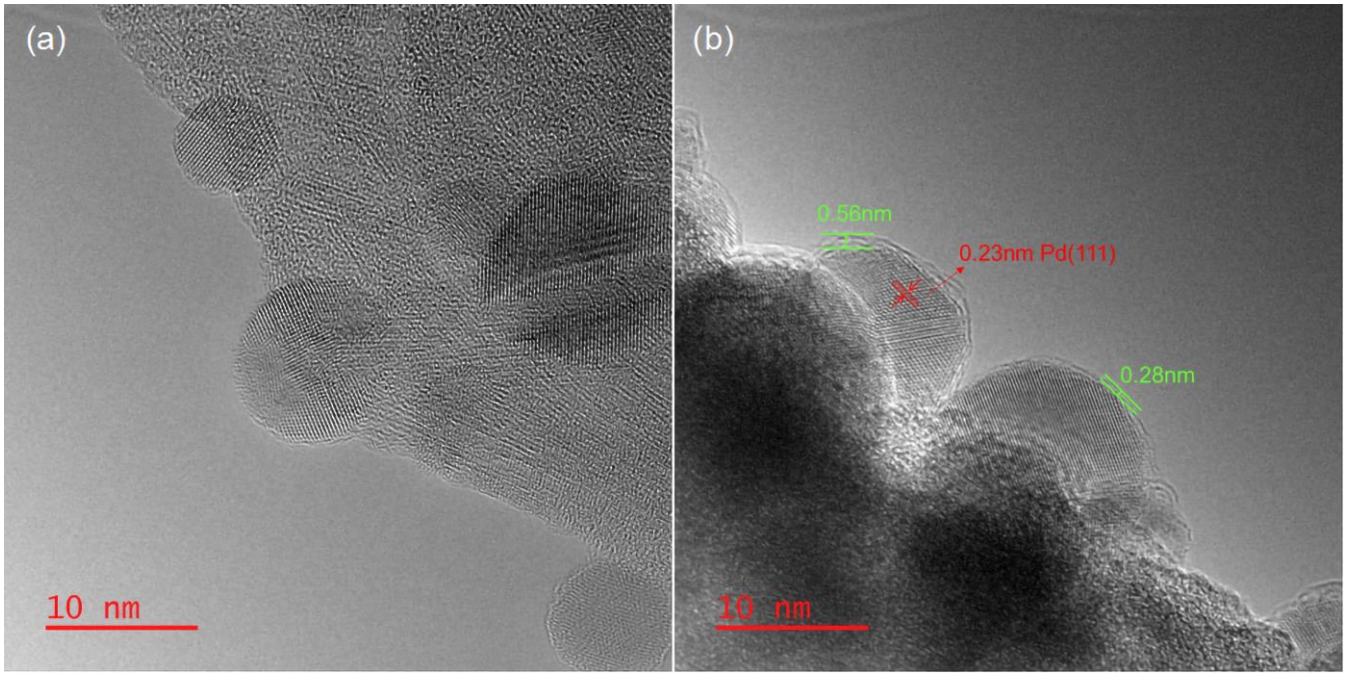


**Fig. 4.** Atomic-resolution TEM images of $Pd/Nb_2O_5$ (a), and $Pd/Nb_2O_5$-500H (b).

of (I) the exterior of the particle, (II) the periphery of the particle, and (III) a region away from the Pd particle. As demonstrated by Fig.3a-3b, no characteristic Nb EELS signal was observed in any of the explored regions in the $Pd/Nb_2O_5$ material. In contrast, an obvious Nb signal was observed in the $Pd/Nb_2O_5$-500H material at the exterior surface of the Pd NPs (I). Furthermore, a smaller, yet visible, Nb signal was observed on the periphery of the Pd particle (II) (Fig. 3d-3e). The diameter of the $NbO_x$ overlayer was subsequently measured and determined to be ca. 0.28 nm (Fig. 4), which is close to the lattice fringe spacing of the $Nb_2O_5$ (101) facet (0.25 nm, Fig. S3-S6). There was however some evidence of bilayered $NbO_x$ at areas close to the metal-support interface. Additional evidence of SMSI in these materials was acquired from room-temperature CO-FTIR experiments. Over the $Pd/Nb_2O_5$ material, bands at ~2080$cm^{-1}$ and 1800-1990 $cm^{-1}$ could be assigned to linear and bridged CO adsorption on Pd NPs, respectively (Fig. 3c) [63-67]. However, for the $Pd/Nb_2O_5$-500H, almost no CO adsorption was observed after argon was introduced to remove any gaseous CO (2173 $cm^{-1}$ and 2116 $cm^{-1}$) [65]. This suggests that CO adsorption onto Pd sites was suppressed by the ultrathin $NbO_x$ overlayer (Fig. 3f).

As previously discussed, SMSI has the potential to modify not only the morphology of supported metal particles but also their properties [68]. For this reason, the series of $Nb_2O_5$-supported Pd materials were probed by electron paramagnetic resonance (EPR) and X-ray photoelectron spectroscopy (XPS). When compared with the other two catalysts, it was clear that the $Pd/Nb_2O_5$-500H material possessed a significantly higher proportion of oxygen vacancies ($O_v$), reaching up to $1.63\times10^{14}$ spins/g (Fig. 6c). The $Pd/Nb_2O_5$-500H material exhibited a large peak at a binding energy of 335.0 eV, which is characteristic of metallic $Pd^0$ NPs, as well as a minor peak at 335.8 eV, indicative of polarised (positively charged) $Pd^{\delta+}$ species [69,70]. The $Pd/Nb_2O_5$ catalysts showed 82.5% $Pd^0$ and 17.5% $Pd^{\delta+}$ over the surface, while an increased ratio of $Pd^{\delta+}$ species (29.9%) was observed in $Pd/Nb_2O_5$-500H due to the existence of SMSI effects in Fig. 6d and Table S2. The presence of $Pd^0$ nanoparticles inevitably led to the hydrogenation of both the C=O group and the furan ring. This observation aligns well with the catalytic performance of HMF conversion, where $Pd/Nb_2O_5$-500H demonstrated an enhanced yield of MF. In contrast, the $Pd/Nb_2O_5$-500H-300O material exhibited a large peak at a binding energy of 336.8 eV, which is characteristic

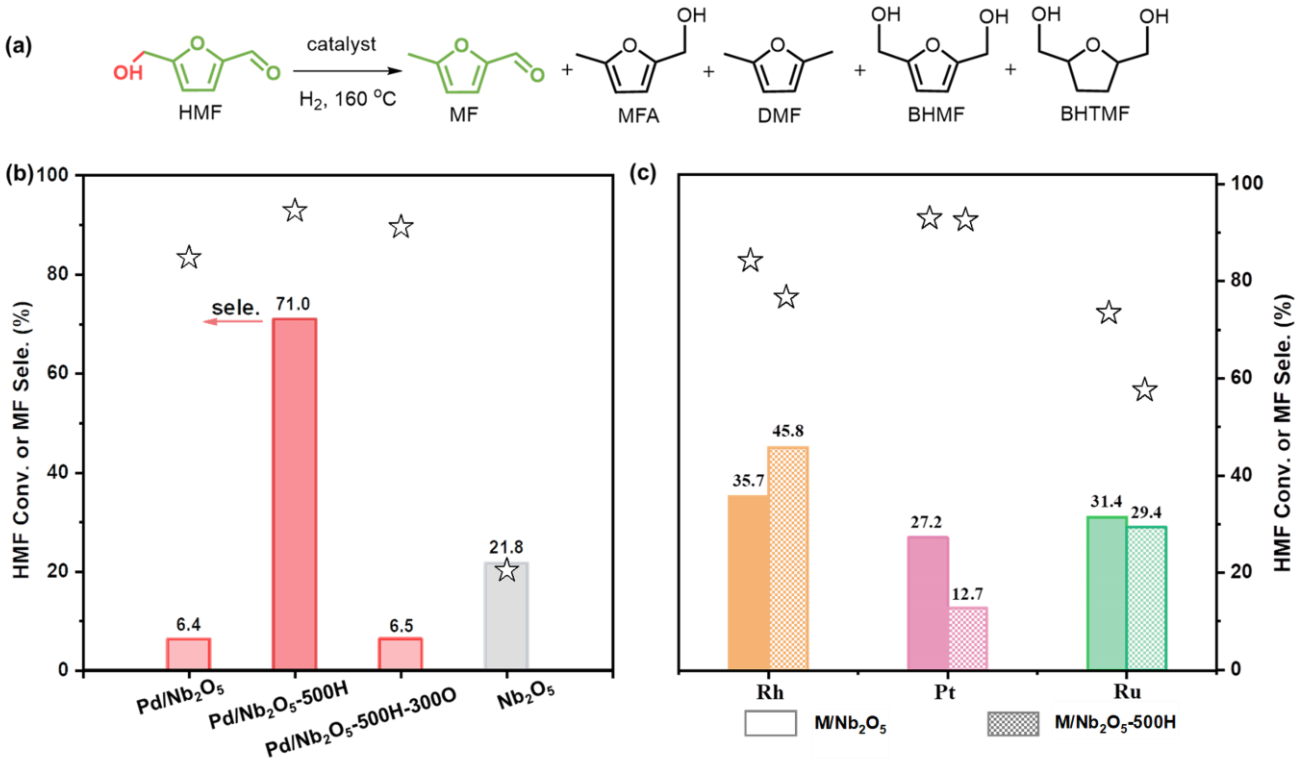


**Fig. 5.** Chemoselective hydrogenolysis of HMF to MF over $Nb_2O_5$-based catalysts. Reaction condition: substrate (12.6 mg), catalyst (10.0 mg), THF (2.0ml), dodecane (15.1mg), $H_2$ (4.0 MPa), 160 °C, 4 h. *Ru/$Nb_2O_5$-500H (5.0 mg): substrate (12.6 mg), THF (2.0ml), dodecane (15.1mg), $H_2$ (4.0 MPa), 160 °C, 4 h.

of PdO.These findings are consistent with the XRD patterns observed for each material, where the Pd/$Nb_2O_5$ and Pd/$Nb_2O_5$-500H materials display diffraction peaks characterizing Pd (111) while the Pd/$Nb_2O_5$-500H-300O exhibits characteristic diffraction peaks of PdO (101) (Fig. S2).

### *3.2. Catalytic performances*

Following the characterization of these materials, they were subsequently assessed as catalysts for the hydrodehydroxylation of HMF to MF (Fig. 5a) in the presence of $H_2$. The results from these experiments are presented in Fig. 5b. The Pd/$Nb_2O_5$ catalyst exhibited an exceptionally poor MF selectivity, reaching only ~ 6% at an HMF conversion of 83.0%. By comparison, the Pd/$Nb_2O_5$-500H catalyst exhibited an MF selectivity of 71.0% at 93.0% HMF conversion. The significant enhancement in MF selectivity (over 11 times higher) hydrodehydroxylation of HMF to MF (Fig. 5a) in the presence of $H_2$. The Pd/$Nb_2O_5$ catalyst exhibited an exceptionally poor MF highlighting how influential the $NbO_x$ overlayer is on the observed catalysis. This was further evidenced by the performance of the analogous calcined catalyst (Pd/$Nb_2O_5$-500H-300O) which exhibited an MF selectivity of 6.5% at an HMF conversion of 90.0 %. We attribute this notable drop in MF selectivity (after the calcination process) to the disappearance of the $NbO_x$ overlayer (Fig. 2k-o).

After observing the favorable performance of Pd/$Nb_2O_5$-500H, we conducted investigations to determine the optimal reaction conditions by varying metal loading, substrate loading, solvent, temperature, and pressure (Fig. S7 and Table S3). Additionally, we assessed the stability of the Pd/$Nb_2O_5$-500H catalyst, as shown in Fig. S8. The cycle experiments demonstrated consistent selectivity over five cycles, although the conversion rate gradually decreased. However, the catalytic performance can be recovered by treatment the spent catalyst at Pd/$Nb_2O_5$-500H under $H_2$/Ar atmosphere (Fig. S9). Interestingly, we found that the Pd/$Nb_2O_5$-500H catalyst also showed good performance for the conversion of HMF in crude HMF-rich biomass hydrolysates and the selectivity of MF could reach

60.2%. Furthermore, the conversion of HMF and selectivity for MF remained consistently stable upon subsequent reuse (Fig. S10). Characterization of the spent catalysts using AC-HAADF-STEM and EELS revealed that the $NbO_x$ overlayer remained intact even after the reaction (Fig. S11).

To evaluate the impact of thermal reduction temperature on $NbO_x$-supported catalysts, aliquots of $Pd/Nb_2O_5$ samples were subjected to reduction at different temperatures. The resulting set of $Pd/Nb_2O_5$-TH materials (TH = 300H, 400H, 500H, 550H, 600H), was further characterized (Fig. S12-S17) and used as catalysts for the hydrodehydroxylation of HMF. The results, presented in Fig. S17, indicate that the reduction temperature had a significant impact on hydrodehydroxylation selectivity; the $Pd/Nb_2O_5$-500H catalyst produced the highest yields of MF. On the contrary, thermal reduction of the $Pd/Nb_2O_5$ material at 300°C and 400°C produced a material that was comparatively poorly selective to hydrodehydroxylation. We propose that was due to the formation of a less defined $NbO_x$ overlayer which was subsequently evidenced by analogous CO-FTIR experiments, which showed that CO chemisorption to Pd NPs was observed in these materials (Fig. S12). $Pd/Nb_2O_5$-600H also exhibited lower selectivity for MF than $Pd/Nb_2O_5$-500H. XRD analysis (Fig. S13) showed that two new peaks were observed at theta = 28.4° and 36.7° on $Pd/Nb_2O_5$-600H indicating the phase transition from the pseudohexagonal (TT) phase to the orthorhombic (T) phase, aligning with previous findings [31,33]. Additionally, $H_2$-TPD (Fig. S15) showed a similar chemisorption amount of hydrogen, indicating that the ultrathin $NbO_x$ layer is permeable to hydrogen, but inaccessible to CO molecules, as previously reported by Christopher [63-66]. These results are also in agreement with analogous BET and CO-pulse chemisorption data (Fig. S14, S16), which shows that the specific surface area of $Nb_2O_5$ and the quantity of CO adsorbed decreased.

To assess the generality of this effect, this procedure was repeated with three other supported metals ($M/Nb_2O_5$-500H, where M = Pt, Ru, and Rh). For consistency, these materials were also well characterized using $H_2$-TPR, HAADF-STEM, EELS, CO-FTIR, XPS, and EPR (Fig. S18–S22). The behavior of these materials was very different from the thermally reduced supported Pd catalyst. Importantly, each of the reduced $M/Nb_2O_5$ exhibited both linear and bridged CO chemisorption (Fig. S19) which [64-66], in accordance with our findings of the supported Pd catalysts, is indicative of an incomplete $NbO_x$ overlayer. Furthermore, the $Pd/Nb_2O_5$-500H catalyst exhibited the largest proportion of $O_v$ sites, up to $1.63\times10^{14}$ spins/g (Fig. S22). These findings were supported by the analogous catalytic testing data, whereby MF selectivities of only 45.8%,12.7%, and 29.4% were obtained over the $Rh/Nb_2O_5$-500H, $Pt/Nb_2O_5$-500H, and $Ru/Nb_2O_5$-500H, respectively. These experimental results are consistent with the characterization data and imply that the nature of the supported metal (and the heat treatments invoked) are instrumental in the formation of SMSI in $Nb_2O_5$-supported catalysts.

Table S4 presents the main by-products, specific selectivity data, and carbon balance over different catalytic systems. According to the product distributions, the possible reaction path over $Pd/Nb_2O_5$ and $Pd/Nb_2O_5$-500H was shown in Fig. S23. No product from the furan ring hydrogenation was detected over $Pd/Nb_2O_5$-500H catalysts. Furthermore, pyridine-FTIR showed that there are more acidic sites on the $Pd/Nb_2O_5$ surface compared with $Pd/Nb_2O_5$-500H, leading to a lower carbon balance (Fig. S24, Table S4, and Table S5).

### *3.3. Mechanistic Investigation*

To further elucidate the excellent hydrodehydroxylation performance of the $Pd/Nb_2O_5$-500H catalyst, several additional characterization techniques and control experiments were conducted with this series of catalysts. Low-temperature CO-FTIR

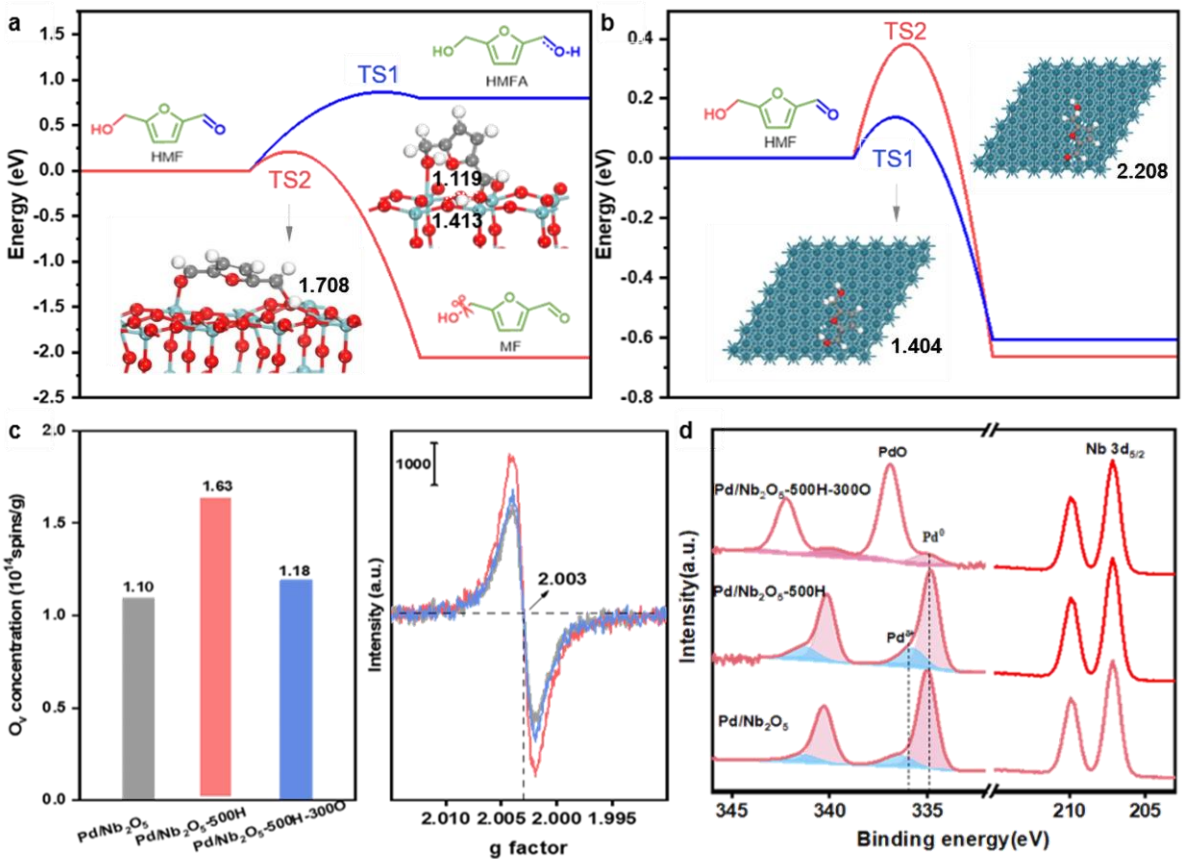


**Fig. 6.** Computational adsorption and conversion of HMF on (a) $Nb_2O_5$ with oxygen vacancy ($O_v$) and (b) Pd (111). The adsorbed HMF can go through two pathways: (1) the CHO hydrogenation (TS1), and (2) the cleavage of the $CH_2$-OH bond (TS2). TS: transition state. (c) Quantitative EPR analysis and (d) XPS analysis of $Pd/Nb_2O_5$, $Pd/Nb_2O_5$-500H, and $Pd/Nb_2O_5$-500H-300O catalysts.

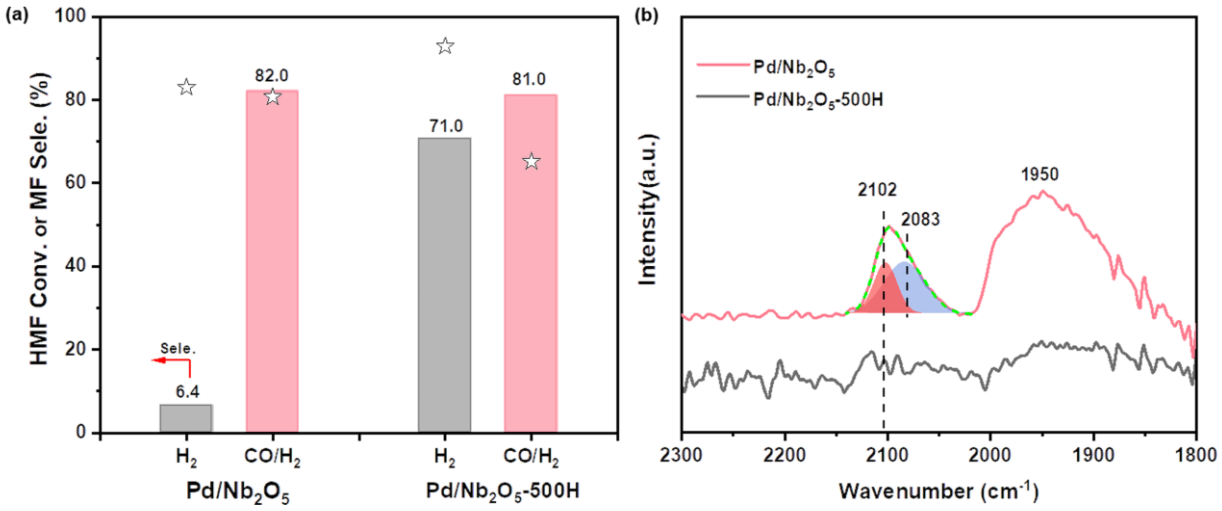


**Fig. 7**. (a) CO poisoning experiments on the catalytic performance of $Pd/Nb_2O_5$ and $Pd/Nb_2O_5$-500H. Reaction condition: substrate (12.6 mg), catalyst (10.0 mg), THF (2.0 mL), dodecane (15.1mg), CO (0.3 MPa), $H_2$ (3.7 MPa), 160 °C, 4 h. (b) Ultralow-temperature CO-pulse FTIR spectra at -150 °C.

experiments were conducted at -150°C, in a pulsed mode, to assess the state of the Pd component. Fig. 7b shows that with the $Pd/Nb_2O_5$ catalyst, adsorption peaks assigned to $Pd_1$ species and Pd NPs are observed at 2102 $cm^{-1}$ and 2083 $cm^{-1}$, respectively. The $Pd/Nb_2O_5$-500H catalyst displays CO adsorption on $Pd_1$ sites, while the intensity of the peak assigned to CO bridging on Pd NPs becomes weak, further implying that most Pd NPs were encapsulated by $NbO_x$. These results indicate that the $Pd/Nb_2O_5$ catalyst has three potential catalytic sites: Pd NPs, $Pd_1$ species, and Nb-$O_v$ sites, whereas the $Pd/Nb_2O_5$-500H only consists of the latter two. To identify the active sites of the catalyst, CO poisoning experiments were performed based on strong CO adsorption on nanoparticles and weak adsorption on a single atom [63]. Upon poisoning, the MF selectivity exhibited by the $Pd/Nb_2O_5$ catalyst led to a 14-fold increase in MF selectivity from 6.4% to 82.0%, while $Pd/Nb_2O_5$-500H only showed a slight increase from 71.0% to 81.0%. These results suggest that Pd nanoparticles are unlikely to be the active site for MF production. Thus, the primary role of the Pd in these materials is to dissociate hydrogen and provide a platform to stabilize defective $NbO_x$ sites (Fig. 7a).

To explore the relationship between reaction selectivity and Nb-$O_v$ sites further, we adopted the use of DFT calculations. The results indicate that HMF can adsorb onto $O_v$ sites on $Nb_2O_5$ through both the OH or CHO moieties; the affiliated adsorption energies were determined to be 2.16 eV and 2.29 eV, respectively. While these two processes possess similar adsorption energies, when HMF adsorbs to $O_v$ through its OH group, is more feasible for the $CH_2$-OH bond to cleave; this process only needs to overcome an energy barrier of 0.21 eV and is strongly exothermic (-2.06 eV) (Fig. 6a). On the contrary, when HMF is adsorbed through the CHO group, it is difficult for it to subsequently undergo hydrogenation; the affiliated energy barrier for this process was calculated to be 0.87 eV. Combining the measured value of oxygen vacancy concentration in Fig.6c with the theoretical calculation of the adsorption difference of HMF at the $O_v$ site, it is fully proved that oxygen vacancies provide more adsorption sites for the OH groups of HMF in the catalytic hydrodeoxygenation reaction. Additionally, it was determined that on Pd(111), HMF can be adsorbed with an adsorption energy of -1.22 eV; the adsorbed HMF can go through two different pathways: (i) the CHO hydrogenation, and (ii) the cleavage of the $CH_2$-OH bond. As shown in Fig. 6b, one can see that the CHO hydrogenation to CHOH on Pd has a very low energy barrier of only 0.14 eV ($\Delta H$ = -0.60 eV), which is 0.24 eV lower than that of the cleavage of the $CH_2$-OH bond (0.38 eV), meaning that, the C=O group of HMF preferentially hydrogenates on Pd NPs, thus leading a poor selectivity to MF production. This result accounts for the low selectivity towards MF observed in the $Pd/Nb_2O_5$ catalyst (Fig. 5b).

## 4. Conclusion

Several characterization techniques have been used to study SMSI that exist between Pd and $Nb_2O_5$ in $Pd/Nb_2O_5$ catalysts. These effects were found to promote the formation of $NbO_x$ overlayers on supported Pd nanoparticles, which was directly observed by electron microscopy. The extent of the $NbO_x$ coverage was determined to be strongly influenced by the thermal reduction conditions that the material was exposed to and was determined to have a significant impact on HMF hydrodehydroxylation selectivity. Mechanistic studies confirmed that the $NbO_x$ overlayer played an important role in the surface mechanism. They were found to: (i) inhibit substrate binding to Pd sites and thus, suppresses undesirable hydrogenation pathways and (ii) promote the formation of oxygen vacancies which promote C–OH dissociation. These results highlight how tailoring SMSI in supported metal catalysts is a highly effective strategy for the development of chemoselective heterogeneous catalysts.

**Declaration of Competing Interest**

The authors declare that they have no known competing financial interests or personal relationships that could have appeared to influence the work reported in this paper.

## Data availability

Data will be made available on request.


## Acknowledgements

This work received financial support from the National Key Research and Development Program of China (2022YFA1504901), the National Natural Science Foundation of China (22293020, 22293022, 22179132, 22121002, 22293012, 22302209), and the Junior Fellowship of Beijing National Laboratory of Molecular Science (2021BMS20059).


### References


[1] J. Zhou, Z. Gao, G. Xiang, T. Zhai, Z. Liu, W. Zhao, X. Liang, L. Wang, Interfacial compatibility critically controls Ru/$TiO_2$ metal-support interaction modes in $CO_2$ hydrogenation, Nat. Commun. 13 (2022) 327. https://doi.org/10.1038/s41467-021-27910-4.

[2] J. Luo, H. Yun, A.V. Mironenko, K. Goulas, J.D. Lee, M. Monai, C. Wang, V. Vorotnikov, C.B. Murray, D.G. Vlachos, P. Fornasiero, R.J. Gorte, Mechanisms for high selectivity in the hydrodehydroxylation of 5-hydroxymethylfurfural over PtCo Nanocrystals, ACS Catal. 6 (7) (2016) 4095-4104. https://doi.org/10.1021/acscatal.6b00750.

[3] B. Zhang, W. Zhou, J. Zhang, Z. Gao, D. Cheng, L. Tang, X. Liu, Y. Song, C. Dong, Y. Xu, J. Yan, M. Peng, H. Liu, M. Douthwaite, M. Wang, D. Ma, Adjacent Pt nanoparticles and sub-nanometer $WO_x$ clusters determine catalytic isomerization of $C_7H_{16}$, CCS Chem. 4 (8) (2022) 2639-2650. https://doi.org/10.31635/ccschem.021.202101454.

[4] J. Zhang, B. Wang, E. Nikolla, W.J. Medlin, Directing reaction pathways through controlled reactant binding at Pd–$TiO_2$ Interfaces, Angew. Chem. Int. Ed. 56 (23) (2017) 6594–6598. https://doi.org/10.1002/anie.201703669.

[5] J. Li, Y. Lin, X. Pan, D. Miao, D. Ding, Y. Cui, J. Dong, X. Bao, Enhanced $CO_2$ methanation activity of Ni/Anatase catalyst by tuning strong metal−support interactions, ACS Catal. 9 (7) (2019) 6342−6348. https://doi.org/10.1021/acscatal.9b00401.

[6] M. Macino, J.A. Barnes, M.S. Althahban, R. Qu, K.E. Gibson, J.D. Morgan, J.S. Freakley, N. Dimitratos, J.C. Kiely, X. Gao, M.A. Beale, B. Donald, Q. He, M. Sankar, and J.D. Hutchings, Tuning of catalytic sites in Pt/$TiO_2$ catalysts for the chemoselective hydrogenation of 3-nitrostyrene, Nat. Catal. 2 (10) (2019) 873-881. https://doi.org/10.1038/s41929-019-0334-3.

[7] G. Kim, S. Shin, Y. Choi, J. Kim, G. Kim, K.J. Kim, and H. Lee, Gas-permeable iron-doped ceria shell on Rh nanoparticles with high activity and durability, J. Am. Chem. Soc. 2 (5) (2022) 1115−1122. https://doi.org/10.1021/jacsau.2c00035.

[8] S.J. Tauster, S.C. Fung, R.L. Garten, Strong metal-support interactions. Group 8 noble metals supported on $Ti0_2$, J. Am. Chem. Soc. 100 (1) (1978) 170-175. https://doi.org/10.1021/ja00469a029.

[9] S.J. Tauster, S.C. Fung, R.T.K. Baker, J.A. Horsley, Strong interactions in supported-metal catalysts, Science 211 (4487) (1981) 1121-1125. https://doi.org/10.1126/science.211.4487.1121.

[10] S.J. Tauster, Strong metal-support interactions, Acc. Chem. Res. 20 (11) (1987) 389-394. https://doi.org/10.1021/ar00143a001.

[11] J. Zhang, H. Wang, L. Wang, S. Ali, C. Wang, L. Wang, X. Meng, B. Li, D. Sheng, F.S. Xiao, Wet-chemistry metal-support interactions in titania-supported Au catalysts, J. Am. Chem. Soc. 141 (7) (2019) 2975−2983. https://doi.org/10.1021/jacs.8b10864.

[12] H. Tang, Y. Su, B. Zhang, A.F. Lee, M.A. Isaacs, K. Wilson, L. Li, Y. Ren, J. Huang, M. Haruta, B. Qiao, X. Liu, C. Jin, D. Su, J. Wang, T. Classical strong metal–support interactions between gold nanoparticles and titanium dioxide, Sci. Adv. 3 (10) (2017) e1700231. https://doi.org/10.1126/sciadv.1700231.

[13] H. Xin, L. Lin, R. Li, D. Li, T. Song, R. Mu, Q. Fu, X. Bao, Overturning $CO_2$ hydrogenation selectivity with high activity via reaction-induced strong metal−support interactions, J. Am. Chem. Soc. 144 (11) (2022) 4874−4882. https://doi.org/10.1021/jacs.1c12603.

[14] H. Tang, J. Wei, F. Liu, B. Qiao, X. Pan, L. Li, J. Liu, J. Wang, T. Zhang, Strong metal-support interactions between gold nanoparticles and Nonoxides, J. Am. Chem. Soc. 138 (1) (2016) 56-59. https://doi.org/10.1021/jacs.5b11306.

[15] J.C. Matsubu, S. Zhang, L. DeRita, N.S. Marinkovic, J.G. Chen, G.W. Graham, X. Pan, P. Christopher, Adsorbate-mediated strong metal-support interactions in oxide-supported Rh catalysts, Nat. Chem. 9 (2) (2017) 120-127. https://doi.org/10.1038/nchem.2607.

[16] H. Chen, Z. Yang, X. Wang, F. Polo-Garzon, W.P. Halstenberg, T. Wang, X. Suo, S.Z. Yang, M.H. Meyer, Z. Wu, and S. Dai, Photoinduced strong metal−support interaction for enhanced catalysis, J. Am. Chem. Soc. 143 (23) (2021) 8521−8526. https://doi.org/10.1021/jacs.0c12817.

[17] T. Pu, W. Zhang, M. Zhu, Engineering heterogeneous catalysis with strong metal-support interactions: characterization, theory and manipulation, Angew. Chem. Int. Ed. 62 (4) (2022) e202212278. https://doi.org/10.1002/anie.202212278.

[18] Z. Luo, G. Zhao, H. Pan, W. Sun, Strong metal–support interaction in heterogeneous catalysts, Adv. Energy Mater. 12 (37) (2022) 202201395. https://doi.org/10.1002/aenm.202201395.

[19] J. Zhang, J. Ma, T.S. Choksi, D. Zhou, S. Han, Y.F. Liao, H.B. Yang, D. Liu, Z. Zeng, W. Liu, X. Sun, T. Zhang, B. Liu, Strong metal−support interaction boosts activity, selectivity, and stability in electrosynthesis of $H_2O_2$, J. Am. Chem. Soc. 144 (5) (2022) 2255-2263. https://doi.org/10.1021/jacs.1c12157,

[20] B. Han, Y. Guo, Y. Huang, W. Xi, J. Xu, J. Luo, H. Qi, Y. Ren, X. Liu, B. Qiao, T. Zhang, Strong metal–support interactions between Pt single atoms and $TiO_2$, Angew. Chem. Int. Ed. 59 (29) (2020) 11824-11829. https://doi.org/10.1002/anie.202003208.

[21] Y. Guo, Y. Li, X. Du, L. Li, Q. Jiang, B. Qiao, Pd single-atom catalysts derived from strong metal–support interaction for selective hydrogenation of acetylene, Nano Res. 15 (12) (2022) 10037–10043. https://doi.org/10.1007/s12274-022-4376-5.

[22] T.W. Van Deelen, M.C. Hernández, K.P.de. Jong, Control of metal-support interactions in heterogeneous catalysts to enhance activity and selectivity, Nat. Catal. 2 (11) (2019) 955-970. https://doi.org/10.1038/s41929-019-0364-x.

[23] Y. Yang, D. Wu, R. Li, P. Rao, J. Li, P. Deng, J. Luo, W. Huang, Q. Chen, Z. Kang, Y. Shen, X. Tian, Engineering the strong metal support interaction of titanium nitride and ruthenium nanorods for effective hydrogen evolution reaction, Appl. Catal. B-Environ. 317 (2022) 121796. https://doi.org/10.1016/j.apcatb.2022.121796.

[24] M. Monai, K. Jenkinson, A.E. Melcherts, L.E.A. Irmak, S.V. Aert, T. Altantzis, C. Vogt, W. Stam, T. Duchon, B. Šmíd, E. Groeneveld, P. Berben, S. Bals, B.S. Weckhuysen, Restructuring of titanium oxide overlayers over nickel nanoparticles during catalysis, Science 380 (6645) (2023) 644–651. https://doi.org/10.1126/science.adf6984.

[25] M. Xu, S. He, H. Chen, G. Cui, L. Zheng, B. Wang, M. Wei, $TiO_{2-x}$-Modified Ni Nanocatalyst with Tunable Metal−Support Interaction for Water−Gas Shift Reaction, ACS Catal. 7 (11) (2017) 7600-7609. https://doi.org/10.1021/acscatal.7b01951.

[26] L. Yan, Q. Zhang, W. Deng, Q. Zhang, Y. Wang, Catalytic valorization of biomass and bioplatforms to chemicals through deoxygenation, ADV CATAL. 66 (2020) 1–108. https://doi.org/10.1016/bs.acat.2020.09.002.

[27] G. Sun,[a] J. An,[a] H. Hu,[a] C. Li,*[b] S. Zuo[a] and H. Xia, Green catalytic synthesis of 5-methylfurfural by selective hydrogenolysis of 5-hydroxymethylfurfural over size-controlled Pd nanoparticle catalysts, Catal. Sci. Technol. 9 (5) (2019) 1238-1244. https://doi.org/10.1039/C9CY00039A.

[28] B. Pomeroy, M. Grilc and B. Likozar, Process condition-based tuneable selective catalysis of hydroxymethylfurfural (HMF) hydrogenation reactions to aromatic, saturated cyclic and linear poly-functional alcohols over Ni–Ce/$Al_2O_3$, Green Chem. 23 (20) (2021) 7996-8002. https://doi.org/10.1039/D1GC02086B.

[29] J. Slak[a], B. Pomeroy[a], A. Kostyniuk[a,*], M. Grilc[a], B. Likozar, A review of bio-refining process intensification in catalytic conversion reactions, separations and purifications of hydroxymethylfurfural (HMF) and furfural, Chem. Eng. J. 429 (2022) 132325. https://doi.org/10.1016/j.cej.2021.132325.

[30] B. Pomeroy[a], M. Grilc[a], S. Gyergyek [b], B. Likozar, Catalyst structure-based hydroxymethylfurfural (HMF) hydrogenation ,mechanisms, activity and selectivity over Ni, Chem. Eng. J. 412 (2021) 127553. https://doi.org/10.1016/j.cej.2020.127553.

[31] Y. Zhao[1,2], X. Zhou[1], L. Ye[3] and S. C. E. Tsang, Nanostructured $Nb_2O_5$ catalysts, Nano Rev. 13 (1) (2012) 1-11. https://doi.org/10.3402/nano.v3i0.17631.

[32] S. H. Chai, H.P. Wang, Y. Liang, B.Q. Xu, Sustainable production of acrolein: Gas-phase dehydration of glycerol over $Nb_2O_5$ catalyst, J. Catal. 250 (2) (2007) 342–349, https://doi.org/10.1016/j.jcat.2007.06.016.

[33] I. Nowak and M. Ziolek*, Niobium Compounds: Preparation, Characterization, and Application in Heterogeneous Catalysis, Chem. Rev. 99 (12) (1999) 3603−3624. https://doi.org/10.1021/cr9800208.

[34] S. Li, J. Du, B. Zhang, Y. Liu, Q. Mei, Q. Meng, M. Dong, J. Du, Z. Zhao, L. Zheng, B. Han, M. Zhao, H. Liu, Selective hydrogenation of 5-(hydroxymethyl)furfural to 5-methylfurfural by exploiting the synergy between steric hindrance and hydrogen spillover, Acta Phys.-Chim. Sin. 38 (10) (2022) 2206019. https://doi.org/10.3866/PKU.WHXB202206019.

[35] A. Jouve, S. Cattaneo, D. Delgado, N. Scotti, C. Evangelisti, J.M.L. Nieto, L. Prati, Furfural hydrogenation on modified niobia, Appl. Sci. 9 (2019). https://doi.org/10.3390/app9112287.

[36] M. E. Jung and G.Y. Jamie Im, Total Synthesis of Racemic Laurenditerpenol, an HIF-1 Inhibitor, J. Org. Chem. 74 (22) (2009) 8739–8753. https://doi.org/10.1021/jo902029x.

[37] C. Ayed,[a, b] W. Huang,[a] G. Kizilsavas,[a] K. Landfester,*[a] and K. A. I. Zhang*[a, c], Photocatalytic Partial Oxidation of 5-Hydroxymethylfurfural (HMF) to 2,5-Diformylfuran(DFF) Over a Covalent Triazine Framework in Water, ChemPhotoChem. 4 (8) (2020) 571-576. https://doi.org/10.1002/cptc.202000070.

[38] A. S. K. Hashmi,* L. Schwarz, P. Rubenbauer, M. C. Blanco, The Condensation of Carbonyl Compounds with Electron-RichArenes: Mercury, Thallium, Gold or a Proton? Adv. Synth. Catal. 348 (6) (2006) 705–708. https://doi.org/10.1002/adsc.200505464.

[39] H. Li, Z. Fang, J. He and S. Yang, Orderly Layered Zr-Benzylphosphonate Nanohybrids for Efficient Acid–Base-Mediated Bifunctional/Cascade Catalysis, ChemSusChem. 10 (4) (2017) 681-686. https://doi.org/10.1002/cssc.201601570.

[40] Y. S. Ren, Z. L. Yuan, K. L. Lv, J. Sun, Z. H. Zhang and Q.Chi, Photocatalytic Partial Oxidation of 5-Hydroxymethylfurfural (HMF) to 2,5-Diformylfuran (DFF) Over a Covalent Triazine Framework in Water, Green Chem. 20 (21) (2018) 4946–4956. https://doi.org/10.1039/C8GC02286K.

[41] B. Liu and Z. H. Zhang, One-Pot Conversion of Carbohydrates into Furan Derivatives via Furfural and 5-Hydroxylmethylfurfural as Intermediates, ChemSusChem. 9 (16) (2016) 2015–2036. https://doi.org/10.1002/cssc.201600507.

[42] B. Liu, Y. S. Ren and Z. H. Zhang, Aerobic oxidation of 5-hydroxymethylfurfural into 2,5-furandicarboxylic acid in water under mild conditions, Green Chem. 17 (3) (2015) 1610–1617. https://doi.org/10.1039/C4GC02019G.

[43] M.E. Jung, G.Y.J. Im, Convergent total synthesis of the racemic HIF-1 inhibitor laurenditerpenol, Tetrahedron Lett. 49 (33) (2008) 4962–4964. https://doi.org/10.1016/j.tetlet.2008.05.116.

[44] W. Wang, X.-M. Zhao, J.-L. Wang, X. Geng, J.-F. Gong, X.-Q. Hao and M.-P. Song, Transition metal-free synthesis of primary amides from aldehydes and hydroxylamine hydrochloride, Tetrahedron Lett. 55 (20) (2014) 3192-3194. https://doi.org/10.1016/j.tetlet.2014.04.020.

[45] K. Michail, V. Matzi, A. Maier, R. Herwig, J. Greilberger, H. Juan, O. Kunert, R. Wintersteiger, Hydroxymethylfurfural: an enemy or a friendly xenobiotic? A bioanalytical approach, Anal. Bioanal. Chem. 387 (8) (2007) 2801–2814. https://doi.org/10.1007/s00216-007-1121-6.

[46] L. Tradtrantip, N.D. Sonawane, W. Namkung, A.S. Verkman, Nanomolar Potency Pyrimido-pyrrolo-quinoxalinedione CFTR Inhibitor Reduces Cyst Size in a Polycystic Kidney Disease Model, J. Med. Chem. 52 (20) (2009) 6447–6455. https://doi.org/10.1021/jm9009873.

[47] S. Li, M. Dong, J. Yang, X. Cheng, X. Shen, S. Liu, Z.Q. Wang, X.Q. Gong, H. Liu, B. Han, Selective hydrogenation of 5-(hydroxymethyl) furfural to 5-methylfurfural over single atomic metals anchored on $Nb_2O_5$, Nat. Commun. 12 (1) (2021) 584. https://doi.org/10.1038/s41467-020-20878-7.

[48] M. S. Ahmad,[a,b] T. Kodama,[c] Y. Nagata,[c] K. Masumoto,[c] K. Sonda,[c] Y. Inomata,[c] K. Hatakeyama,[c] A. T. Quitain,[c] A. Shotipruk,[d] and T. Kida [*a,b,c], Selective hydrogenation of 5-hydroxymethyl furfural to 5-methyl furfural over graphene oxide supported Mn nanoparticles, Doi: 10.2139/ssrn.4496864.

[49] L. Dong, M.V. Jordi, L. Mu, L. Li, N. Lopezb, P.R. Javier. Z. Chen, Selective hydrogenolysis of 5-hydroxymethylfurfural to 5-methylfurfural over $Au/TiO_2$, Appl. Catal. B Environ. 335 (2023) 122893. https://doi.org/10.1016/j.apcatb.2023.122893.

[50] S. Vichaphund, D. Aht-ong, V. Sricharoenchaikul, D. Atong, Effect of crystallization temperature on the in situ valorization of physic nut (Jatropha curcus L.) wastes using synthetic HZSM-5 catalyst, Chem Eng Res Des. 92 (10) (2014) 1883–1890. https://doi.org/10.1016/j.cherd.2014.05.013.

[51] A.M. Barriosa, C.A. Telesa, P.M. de Souzaa, R.C. Rabelo-Netoa, C. Raimundo, D. Gary Jacobsc, H. Burtron, L.E.P. Borgesb, F.B. Noronha, Hydrodeoxygenation of phenol over niobia supported Pd catalyst, Catal Today. 302 (2018) 115–124. http://dx.doi.org/10.1016/j.cattod.2017.03.034.

[52] E.I. Ko, J.M. Hupp, F.H. Rogan, and N.J. Wagner. Preparation, reduction, and chemisorption behavior of niobia-supported nickel catalysts, J. Catal. 84 (1) (1983) 85-94. https://doi.org/10.1016/0021-9517(83)90088-X.

[53] R. Huang, O. Kwona, C. Lina, R.J. Gorte, The effects of SMSI on m-Cresol hydrodeoxygenation over $Pt/Nb_2O_5$ and $Pt/TiO_2$, J. Catal. 398 (2021) 102–108. https://doi.org/10.1016/j.jcat.2021.04.012.

[54] E.I. Ko, J.M. Hupp, and N.J. Wagner. Activity and selectivity of a niobia ($Nb_2O_5$)-supported nickel catalyst in CO hydrogenation, J. Chem. Soc. Chem. Commun. (2) (1983) 94-95. https://doi.org/10.1039/C39830000094.

[55] T. Chen, and J.M. Vohs, Direct hydrodeoxygenation of m-Cresol to toluene over bifunctional NbOx−Pt, J. Phys. Chem. C. 124 (26) (2020) 14253−14261. https://dx.doi.org/10.1021/acs.jpcc.0c03988.

[56] M. Ziolek, Niobium-containing catalysts—the state of the art, Catal. Today. 78 (1-4) (2003) 47-64. https://doi.org/10.1016/S0920-5861(02)00340-1.

[57] Z. Karpiński, M. Bonarowska, D. Łomot, P.D. Śrębowata, J.A.R. Costa, Hydrogenolysis of carbon–halogen and carbon–carbon bonds over $Pd/Nb_2O_5–Al_2O_3$ catalysts, Catal. Commun. 10 (13) (2009) 1757-1761. https://doi.org/10.1016/j.catcom.2009.05.024.

[58] G. Kresse, J. Furthmüller, Efficient iterative schemes for Ab Initio total-energy calculations using a plane-wave basis set, Phys. Rev. B. 54 (16) (1996) 11169-11186. https://doi.org/10.1103/PhysRevB.54.11169.

[59] J. P. Perdew, A. Ruzsinszky, G. I. Csonka, O. A. Vydrov, G. E. Scuseria, L. A. Constantin, X. Zhou, K. Burke, Restoring the density-gradient expansion for exchange in solids and surfaces, Phys. Rev. Lett. 100 (13) (2008) 136406. https://doi.org/10.1103/PhysRevLett.100.136406.

[60] G. Kresse, D. Joubert, From ultrasoft pseudopotentials to the projector augmented-wave method, Phys. Rev. B. 59 (3) (1999) 1758-1775. https://doi.org/10.1103/PhysRevB.59.1758.

[61] A. Alavi, P. Hu, T. Deutsch, P.L. Silvestrelli, J. Hutter, J. CO oxidation on Pt(111): an Ab Initio density functional theory study, Phys. Rev. Lett. 80 (16) (1998) 3650-3653. https://doi.org/10.1103/PhysRevLett.80.3650.

[62] Y. Zhang, W. Yan, H. Qi, X. Su, Y. Su, X. Liu, L. Li, X. Yang, Y. Huang, and T. Zhang, Strong metal−support Interaction of Ru on $TiO_2$ derived from the Co-reduction mechanism of $RuxTi_1−xO_2$ interphase, ACS Catal. 12 (3) (2022) 1697−1705. https://doi.org/10.1021/acscatal.1c04785.

[63] C. F. Meunier, Relevance of IR spectroscopy of adsorbed CO for the characterization of heterogeneous catalysts containing isolated atoms, J. Phys. Chem. C. 125 (40) (2021) 21810−21823. https://doi.org/10.1021/acs.jpcc.1c06784.

[64] B.C. Gates, Atomically dispersed supported metal catalysts: seeing Is believing, Trends Chem. 1 (1) (2019) 99-110. https://doi.org/10.1016/j.trechm.2019.01.004.

[65] Y. Tang, C. Asokan, M. Xu, G.W. Graham, X. Pan, P. Christopher, J. Li, P. Sautet, Rh single atoms on $TiO_2$ dynamically respond to reaction conditions by adapting their site, Nat. Commun. 10 (2019) 4488. https://doi.org/10.1038/s41467-019-12461-6.

[66] X. Li, X.I. Pereira-Hernández, Y. Chen, J. Xu, J. Zhao, C.W. Pao, C.Y. Fang, J. Zeng, Y. Wang, B.C. Gates, J. Liu, Functional CeOx nanoglues for robust atomically dispersed catalysts, Nature 611 (7935) (2022) 284–288. https://doi.org/10.1038/s41586-022-05251-6.

[67] Y. Guo, Y. Huang, B. Zeng, B. Han, M. AKRI, M. Shi, Y. Zhao, Q. Li, Y. Su, L. Li, Q. Jiang, Y.T. Cui, L. Li, R.Li, B. Qiao, & T. Zhang, Photo-thermo semi-hydrogenation of acetylene on $Pd_1/TiO_2$ single-atom catalyst, Nat. Commun. 13 (1) (2022) 2648. https://doi.org/10.1038/s41467-022-30291-x.

[68] Y. Zhang, J.X. Liu, K. Qian, A. Jia, D. Li, L. Shi, J. Hu, J. Zhu, and W. Huang, Structure sensitivity of Au-$TiO_2$ strong metal–support Interactions, Angew. Chem. Int. Ed. 60 (21) (2021) 12074-12081. https://doi.org/10.1002/anie.202101928.

[69] C. Dong, Z. Gao, Y. Li, M. Peng, M. Wang, Y. Xu, C. Li, M. Xu, Y. Deng, X. Qin, F. Huang, X. Wei, Y.G. Wang, H. Liu, W. Zhou, D. Ma, Fully exposed palladium cluster catalysts enable hydrogen production from nitrogen heterocycles, Nat. Catal. 5 (6) (2022) 485–493, https://doi.org/10.1038/s41929-022-00769-4.

[70] J.E. Benson, H.S. Hwang, M. Boudart, Hydrogen-oxygen titration method for the measurement of supported palladium surface areas, J. Catal. 30 (1) (1973) 146-153, https://doi.org/10.1016/0021-9517(73)90061-4.